7 - 12 SEPTEMBER 2014, KRAKÓW
FORUM ACUSTICUM

Finite element modeling of the vocal folds with deformable interface tracking

Alba Granados, Jonas Brunskog
Department of Electrical Engineering, Technical University of Denmark.

Marek Krzysztof Misztal
The Niels Bohr Institute, University of Copenhagen, Denmark.

Vincent Visseq, Kenny Erleben
Department of Computer Science, University of Copenhagen, Denmark.

Summary
Continuous and prolonged use of the speaking voice may lead to functional speech disorders that are not apparent for voice clinicians from high-speed imaging of the vocal folds' vibration. However, it is hypothesized that time dependent tissue properties provide some insight into the injury process. To infer material parameters via an inverse optimization problem from recorded deformation, a self sustained theoretical model of the vocal folds is needed. With this purpose, a transversely isotropic three-dimensional finite element model is proposed and investigated. Special attention is paid to the collision and time integration schemes. Accuracy in the deformation process is introduced by means of a topology-adaptive method for deformable interface tracking, called the Deformable Simplicial Complex, which has been previously applied to immiscible fluids. For computational reasons, aerodynamic driving forces are derived from Bernoulli's principle.

PACS no. 43.70.Aj, 43.70.Bk, 43.70.Jt

1. Introduction

In contrast to organic voice problems, vocal folds vibrations of individuals suffering from functional voice problems are not visually impaired, making it difficult to objectively prove an abnormal voice health [1]. Consequently, voice clinician have very little insight on the processes of injury, healing and recovery of the tissue. However, considerable research on voice disorders by means of high-speed images techniques has taken place in recent years [2, 3]. This research field may potentially provide tools to infer characteristics of vocal folds with functional dysfunction.

The use of high-speed images to analyze aspects of phonation may require an inverse analysis involving a biomechanical model of the vocal folds [4]. A large number of vocal folds models have been studied in the last sixty years; from simplistic lumped-mass solid models driven by a Bernoulli flow [5], to sophisticated Navier-Stokes turbulent flows coupled to a solid structure [6]. For computational reasons, a simplified model is desired for inverse problem formulations. Nevertheless, the need of accuracy within the vocal fold tissue for functional voice problems investigation, suggests the use of a continuum model. Therefore, in the current work, a Bernoulli flow model coupled to a continuum 3-dimensional model of the vocal folds is presented.

Numerical solutions of the equations of motion include the application of temporal discretization schemes. These schemes can alter the accuracy of the solution, and therefore introduce numerical dispersion or dissipation [7]. In inversion analysis based on vibration patterns, unphysical artifacts of the discretization process may be undesirable. Most of the existing vocal folds models perform the temporal integration by means of high-order Runge-Kutta [2], central difference [8], or Newmark [9] schemes. In the present work, a simulation study on the importance of the temporal schemes is presented.

When vocal folds vibrate at normal speaking frequencies, collisions occur. This phenomena has been mainly modeled by a Herzian approach, and by enforcing position based constrains. The numerics and formulations behind the later approach is an active field of research in the contacts mechanics community. The present work intends to contribute to a better understanding of vocal folds collision. A model for asymmetric contact is presented in an effort to provide tools for voice health diagnosis.

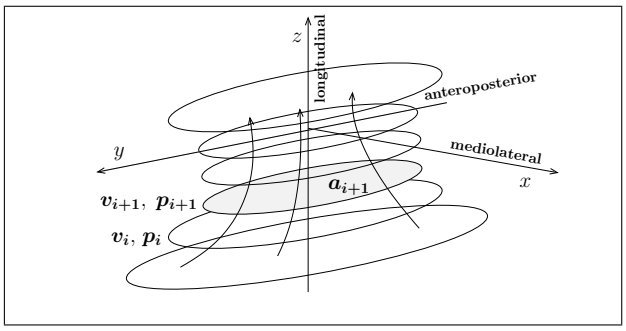

Figure 1. Schema of the larynx. The index i defines the ith cross section area.

Studying the numerical aspects of vocal folds models requires a computer framework that allows for user's modifications. The present model is implemented within the Deformable Simplicial Complex framework [10], which has been successfully applied to immiscible fluids.

2. Fluid-Structure Model

2.1. Airflow

For an incompressible fluid with constant density ρ_{air} and no-slip condition at the boundary, the Bernoulli flow equation applied to the glottal canal yields the relation

$$p_{i+1} = p_i + \frac{\rho_{air}}{2} U^2 \left(\frac{1}{a_i^2} - \frac{1}{a_{i+1}^2} \right) \tag{1}$$

where average flow velocities have been assumed through the transverse cross section areas a_i and a_{i+1}, $U = U(t)$ is the volumetric flow rate, and p_i are aerodynamic pressures; see figure 1. No energy loss is considered neither at glottal inlet nor outlet [11]. Assuming a negligible subglottal kinetic energy, as well as no vocal tract coupling, the volumetric flow rate may be approximated as

$$U = \sqrt{\frac{2P_s}{\rho_{air}}} a_{det} \tag{2}$$

where P_s is the subglottal pressure, and a_{det} is the cross section where the flow detaches from the vocal folds boundaries. Previous studies have investigated flow separation models, e.g. Ref. [12]. In the present work, the flow detaches from the boundary at minimum cross sectional area $a_{det} = a_{min}$; upstream that point, a jet is formed.

By spatial discretization of the vocal folds' boundary, the transversal areas a_i in Eq. 1 are computed by assuming an elliptical shape, as in Ref. [9]. In the present study, the computation takes into account asymmetrical mediolateral deformation of the vocal folds by allowing for independent minor axis, that is,

$$a_i = \frac{\pi}{2} y_i (x_i^r + x_i^l) \tag{3}$$

where y_i is the major axis in the anteroposterior direction, and x_i^r and x_i^l are the right and left minor axes in the mediolateral direction.

2.2. Tissue

2.2.1. Governing and Constitutive Equations

Under deformation of a body a material particle is displaced from its original position $\mathbf{X} \in V_{\text{solid}} \subset \mathbb{R}^3$ (material coordinates) to its current position $\varphi(\mathbf{X}) = \mathbf{x} \in v_{\text{solid}} \subset \mathbb{R}^3$ (spatial coordinates) via the deformation mapping $\varphi : V_{\text{solid}} \to \mathbb{R}^3$. The displacement field $\mathbf{u}(\mathbf{X}, t) = \mathbf{x} - \mathbf{X}$ in a Lagrangian representation is thereby determined. From basic continuum mechanics, the motion of the body is described by

$$\nabla \cdot \boldsymbol{\sigma} = \rho \frac{\partial^2 \mathbf{x}}{\partial t^2} \qquad \forall \mathbf{x} \in v_{\text{solid}} \tag{4}$$

where ρ is the spatial mass density, and $\boldsymbol{\sigma}$ is the Cauchy stress tensor. For the vocal folds, the Cauchy stress tensor at the airflow boundary $\Gamma_n \subset \partial v_{\text{solid}}$ with normal $\mathbf{n}$ satisfies the Neumann condition

$$\boldsymbol{\sigma} \cdot \mathbf{n} = \mathbf{p} \tag{5}$$

where $\mathbf{p} = p_i \mathbf{n}$ from Eq. 1. Dirichlet conditions enforce zero displacement at the anteroposterior glottal extreme points.

It is widely accepted in the voice research community, that vocal folds undertake small displacements during normal phonation [8]. In the present model, the small deformations assumption is also made, and the strain tensor is approximated by the Cauchy's strain tensor $\boldsymbol{\epsilon}$.

The laryngeal tissue is modeled as a compressible viscoelastic Kelvin-Voigt model with stiffness matrix $\mathcal{S}$ described in Ref. [13], and a dynamic viscosity η as in Ref. [9]. The constitutive equation is

$$\boldsymbol{\sigma}(t) = \mathcal{S}\boldsymbol{\epsilon}(t) + \eta \frac{\partial}{\partial t} \boldsymbol{\epsilon}(t) \tag{6}$$

where symmetry of the stress and strain tensors has been assumed.

2.2.2. Collision Modeling

When two moving bodies collide, surface contact kinematic conditions are involved in the dynamics of the system. Even for linear elasticity theory, the inclusion of these conditions puts the transient problem in the complex category of piecewise-smooth dynamics. Therefore, a rigorous mathematical analysis of vocal folds' collision in continuum domains is outside the scope of the present work.

In addition to the boundary conditions connected to the contact-free equilibrium Eq. 4, when collision occurs additional contact boundary conditions on the contact surface $\Gamma_c \subset \partial v_{\text{solid}}$ arise to avoid body interpenetration; these are position based constraints. By assuming frictionless contact, the non-penetration

constraint may be expressed in the current configuration v_{solid} in terms of the normal gap $g_N(\mathbf{x})$ as

$$g_N(\mathbf{x}) = (\mathbf{x}^1 - \mathbf{x}^2) \cdot \mathbf{n}^1 \geq 0 \tag{7}$$

where the superscript indicates each of the colliding bodies [14]. In classic collision literature, the superscript 2 corresponds to the interface slave node that penetrates into the master surface denoted by the superscript 1. The vector $\mathbf{n}^1$ is the normal to the master surface at the point $\mathbf{x}^1$, which is the projection of $\mathbf{x}^2$ onto the master surface. When contact occurs, that is, $g_N(\mathbf{x}) = 0$, a Cauchy traction vector $\mathbf{t}$ is active at the contact point. This reaction force must satisfy the action-reaction principle, and for non-adhesion contact, its normal component $r_N = \mathbf{t} \cdot \mathbf{n}$ must be compressive, i.e., it must be negative. These conditions may be written in a compact form as

$$g_N(\mathbf{x}) \geq 0, \qquad r_N \leq 0, \qquad g_N(\mathbf{x}) r_N = 0 \tag{8}$$

which are known as Signorini conditions for frictionless contact in contact mechanics [14].

In analytic mechanics, the equilibrium equations emanate from the Hamilton's principle, that is, through the process of minimizing a functional $\Pi(\mathbf{v})$ which involves the difference between potential and kinetic energy; see e.g., [15]. The branch of mathematics of calculus of variations provides multiple methodologies to solve a constrained minimization problem, primarily the Lagrange-multiplier and the penalty methods. These methods can be applied to enforce the collision constrains given in relation 8 in exact or relaxed way, respectively. The Lagrangian approach consists of enforcing non-penetration by appending a functional $\lambda \cdot g_N(\mathbf{v})$ to the objective function $\Pi(\mathbf{v})$, with λ being the Lagrange multiplier and $g_N(\mathbf{v})$ defined in Eq. 7. Solution to this problem yields the exact unknown reaction force λ that assures non-penetration. However, one of the drawback to the Lagrange method is the increase of the dimension of the system, by addition of unknowns in the form of Lagrange multiplier. Furthermore, the temporally discrete problem formulation shows that the resulting system matrix is not definite positive, or even singular. Although this can be solved by additional numerical treatment, in general, the classical Lagrange has shown weakness with regards to velocity and contact force calculations [16]. For these reasons, and for the sake of simplicity, the present work intends to investigate a penalty approach to enforce collision constrains.

Allowance of the inter-penetration is widely used in vocal folds literature; see e.g., Ref. [17]. This inter-penetration is a consequence of a penalty method approach to the constrained minimization problem. The method consists of appending a penalty functional to the objective function as

$$\min_{\mathbf{v}} \left\{ \Pi(\mathbf{v}) + \frac{1}{2} \cdot \kappa \cdot \left(g_N(\mathbf{v}) \right)^2 \right\} \tag{9}$$

where the positive scalar κ is the penalty parameter, which is given, and quantifies how severely the non-penetration constraint is violated. The penalty method maintains the dimension of the collision-free problem. Enforcing the non-penetration constrain by increasing the penalty parameters derives in an ill-conditioning of the global matrix. Therefore, the user is required to make a thoughtful choice of the penalty parameter, as in Ref. [18]. In the present work, no thorough investigations on parameter-choice methods are presented, which may be object of future studies.

2.2.3. Spatial and temporal discretization.

For admissible square-integrable test functions $\mathbf{w}$ that vanish at the Dirichlet boundary and satisfy the non-penetration condition given in Eq. 7 at the boundary Γ_c, the problem takes the suitable weak form

$$\int_{V_{\text{solid}}} \rho \mathbf{w}^T \cdot \frac{\partial \mathbf{x}^2}{\partial t^2} \, \mathrm{d}V + \int_{V_{\text{solid}}} \nabla \mathbf{w}^T : \boldsymbol{\sigma} \, \mathrm{d}V + \kappa \int_{\Gamma_c} \mathbf{g}_N(\mathbf{w})^T \cdot \mathbf{g}_N(\mathbf{x}) \, \mathrm{d}S = \int_{\Gamma_n} \mathbf{w}^T \cdot \mathbf{p} \, \mathrm{d}S \tag{10}$$

used as a starting point for the finite element formulation. Spatial gradients and material integrals in Eq. 10 can be mixed as a consequence of the small displacement assumption. Considering the spatial finite element discretization yields the matrix form

$$\mathbf{M}\ddot{\mathbf{x}} + \mathbf{D}\dot{\mathbf{x}} + \left(\mathbf{K} + \kappa \mathbf{G}^T \mathbf{G}\right)\mathbf{x} = \mathbf{F} \tag{11}$$

where $\mathbf{G}$ is the Jacobian of the penetration function given in Eq. 7, and $\mathbf{M}$, $\mathbf{D}$, $\mathbf{K}$ and $\mathbf{F}$ are the mass, damping, stiffness and aerodynamic matrices respectively; dots indicate time derivatives.

For linear approximations defined in a tetrahedral mesh, the system matrices in Eq. 11 can be easily derived by means of isoparametric transformations [7]. In the same way, the aerodynamic linear pressure acting on a triangular face $\partial V^{en}_{\text{solid}} \subset \Gamma_n$ of an element tetrahedron V^{en}_{solid} satisfies

$$F_\alpha = \begin{cases} \frac{\Lambda}{6}(p_A + \frac{p_B}{2} + \frac{p_C}{2}) & \text{if} \quad \alpha = A \\ \frac{\Lambda}{6}(\frac{p_A}{2} + p_B + \frac{p_C}{2}) & \text{if} \quad \alpha = B \\ \frac{\Lambda}{6}(\frac{p_A}{2} + \frac{p_B}{2} + p_C) & \text{if} \quad \alpha = C \end{cases} \tag{12}$$

where p_α are the pressures derived from Eq. 1 applied to each node A, B and C, and Λ stands for the area of the triangular face $\partial V^{en}_{\text{solid}}$. Each force vector $\mathbf{F}_\alpha$ takes the direction of the normal to the interface triangle $\partial V^{en}_{\text{solid}}$.

Besides the difficulties of the parameter-choice problem in penalty formulations, attention has to be paid to temporal discretization methods, since unstabilities and accuracy problems may arise. The most commonly used algorithm to temporally discretize the hyperbolic problem is the implicit Newmark one-step

method [19] as used in Ref. [9]. The method consists of the equations

$$\begin{aligned}\mathbf{x}_{n+1} &= \underbrace{\mathbf{x}_n + h\dot{\mathbf{x}}_n + \frac{h^2}{2}(1-2\beta)\ddot{\mathbf{x}}_n}_{\tilde{\mathbf{x}}_{n+1}} + \beta h^2 \ddot{\mathbf{x}}_{n+1} \\ \dot{\mathbf{x}}_{n+1} &= \underbrace{\dot{\mathbf{x}}_n + (1-\gamma)h\ddot{\mathbf{x}}_n}_{\tilde{\dot{\mathbf{x}}}_{n+1}} + \gamma h \ddot{\mathbf{x}}_{n+1} \end{aligned} \tag{13}$$

where γ and β are the algorithm parameters associated with the quadrature scheme, h is the time step, and $\tilde{\mathbf{x}}_{n+1}$ and $\tilde{\dot{\mathbf{x}}}_{n+1}$ are the so-called predictors. A first naive approach of the temporal discretization, the acceleration $\ddot{\mathbf{x}}_{n+1}$ may be found by recursion as

$$\begin{aligned}(\mathbf{M} + \gamma h \mathbf{D} + h^2 \beta \overline{\mathbf{K}})\ddot{\mathbf{x}}_{n+1} \\ = \mathbf{F}_{n+1} - \mathbf{D}\tilde{\dot{\mathbf{x}}}_{n+1} - \overline{\mathbf{K}}(\tilde{\mathbf{x}}_{n+1} - \mathbf{X})\end{aligned} \tag{14}$$

with $\overline{\mathbf{K}} = \mathbf{K} + \kappa \mathbf{G}^T \mathbf{G}$ when collision occurs, and $\overline{\mathbf{K}} = \mathbf{K}$ otherwise.

The parameters γ and β control accuracy and stability of the scheme, which can be studied by spectral analysis of the amplification matrix [7]. For smooth systems, the condition $2\beta \geq \gamma \geq \frac{1}{2}$ (trapezoidal rule, if equality) assures unconditional stability, that is, for all time steps h it prevents unbounded solutions as n becomes large. If Rayleigh damping is assumed, $\gamma > 1/2$ and $\beta = (\gamma + 1/2)^2/4$ (modified average acceleration) produces an unconditionally stable scheme with numerical dissipation in all frequency range, specially at higher modes, where finite element solution seems to deteriorate. However, the accuracy of the algorithm drops to first order; second-order accuracy is achieved if and only if $\gamma = 1/2$. High accuracy and very low numerical dispersion can be achieved by sacrificing unconditional stability. However, due to wide range of system eigenfrequencies, the time step must be very small in order to assure a stable schema, which makes the algorithm less competitive.

An alternative method with second-order accuracy and numerical damping at high frequencies is the Hilber-Hughes-Taylor α-method [20]. The schema consists of the Newmark equations in Eq. 13 with modified equilibrium equations, which leads to the recursion

$$\begin{aligned}\left[\mathbf{M} + (1+\alpha)\gamma h \mathbf{D} + (1+\alpha)h^2\beta\overline{\mathbf{K}}\right]\ddot{\mathbf{x}}_{n+1} \\ = \mathbf{F}_{n+1} - \mathbf{D}\tilde{\dot{\mathbf{x}}}_{n+1} + \alpha\mathbf{D}\dot{\mathbf{x}}_n - \overline{\mathbf{K}}(\tilde{\mathbf{x}}_{n+1} - \mathbf{X}) \\ + \alpha\overline{\mathbf{K}}(\mathbf{x}_n - \mathbf{X})\end{aligned} \tag{15}$$

where the parameter α controls the amount of numerical dissipation; the smaller, the more wide mode damping is introduced, and the less keeping very little low mode damping. It has been shown that for $\alpha \in [-1/3, 0]$, $\gamma = 0.5 - \alpha$ and $\beta = (1-\alpha)^2/4$, the scheme is unconditionally stable with second-order accuracy. Nevertheless, the scheme introduces a period error larger than the one produced by a trapezoidal rule, with increases as the parameter α is decreased.

It is worthwhile to mention that accuracy analysis have been made by assuming smoothness and homogeneity of the system, as well as small Rayleigh damping [7]. Therefore, computer evaluation is required for the present vocal folds model.

2.3. Deformable Simplicial Complex

The Deformable Simplicial Complex (DSC) method is a topology-adaptive method for tracking deformable interfaces [10]. The 3-dimensional DSC framework represents the interface as a set of triangular faces separating a tetrahedral unstructured mesh in different mediums. It allows interface topology changes between time step, once the finite element system has been solved [21]. The DSC framework has been tested in multiphase flow problems, and it is currently extended to contact solid mechanics problem [22]. In the present work, a new vocal folds' collision mechanisms has been implemented within the DSC framework. The finite element Eq. 11 is solved in a tetrahedral solid mesh. The airway domain is also discretized by tetrahedron-shaped elements, for collision detection purpose.

2.3.1. Deformable Interface Tracking

Collision detection mechanism as well as penetration distance approximation are non-trivial problems in transient contact mechanics. Numerically, the interpenetration integral in Eq. 11 may be approximated by volume interpenetration. However, for a piecewise linear finite element surface, projection of the slave node onto the master surface may lead to existence and uniqueness problems. Additionally, just before collision occurs, degenerated volumetric elements may appear. In vocal folds collision, this problem has been solved by enforcing a minimum volume between vocal folds; see Refs. [23, 24, 25]. However, this approach requires knowing a priori the collision point, usually assumed to be at the midsaggital plane. In speech disorders research, it is important to avoid this assumption, since asymmetries in the vocal folds' dynamics are related to abnormal voice health.

In the present work, contact detection and interpenetration volumes are computed by means of conforming mesh, connecting the two sides of the vocal folds, as shown in figure 2. It allows for asymmetric collision since the contact scheme is based on oriented volume inversion. The contact algorithm may be summarized as follows:

```
 // time -> t
1:  for ('tet' in airway)
2:    if (oriented 'tet' volume V < 0)
3:      for (vertex in 'tet')
4:        penetration = penetration + V/4
5:        force direction =
                  = displacement direction
6:      end for
```

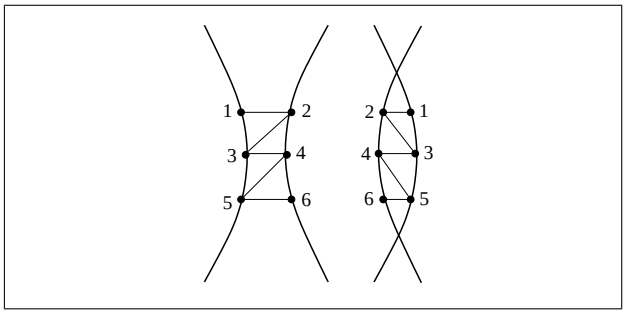

Figure 2. Conforming interface mesh for collision detections; transverse view before collision (left), after collision (right).

```
7:     end if
8:   end for
 // time -> t+dt
```

The algorithm safely avoids the classical master-slave paradigm, since no normal gap computations are needed. The collision force is uniformly distributed within the four boundary vertices (line 4 in the algorithm), which makes the algorithm compatible with the action-reaction principle. The reaction force is parallel to the displacement vector (line 5); this is a reasonable approximation whenever the deformation is not large.

The collision approach is based in a coarse airway mesh, which cannot present inner vertices. Therefore, an obvious drawback of the algorithm is the incompatibility with a numerical Navier-Stokes model of the flow.

3. Simulations

The tissue and air parameters used in the simulations have been adapted from Refs. [9, 24]; see table I. The dimensions and geometry is based on Ref. [9]. Dirichlet conditions enforce zero displacement at the antero-posterior glottal extreme points.

Table I. Tissue parameters for a normal larynx, adapted from Refs. [9, 24]. (E, ν), transversal Young's modulus and Poisson's ratio; (E', μ', ν'), longitudinal Young's and shear modulus, and Poisson's ratio.

Tissue	E [kPa]	ν	E' [kPa]	μ' [kPa]	ν'	η [P]
Cover	1	0.66	10	10	0.66	4
Ligament	3	0.58	20	40	0.58	10
Body	20	0.45	40	30	0.45	10

To a first approximation, the penalty parameter is chosen as $k = 10^6$. However, parameter-choice techniques must be investigated in further studies. The aerodynamic flux is set to zero whenever any of the colliding nodes have y coordinate such that $|y| \leq 0.7/3$.

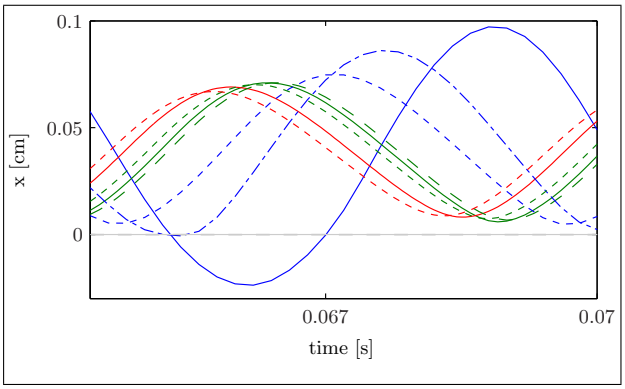

Figure 3. Blue $h = 200\,\mu s$, green $h = 100\,\mu s$, red $h = 50\,\mu s$; solid 'TR', short dashed 'HHT' with $\alpha = -0.3$, long dashed 'HHT' with $\alpha = -0.05$, dot-dashed 'MAA' with $\gamma = 0.6$.

The finite element mesh consists in 24584, 12754 and 17646 tetrahedra for body, ligament and cover, respectively. The layers are labeled differently for the left ($x < 0$) and right ($x > 0$) vocal folds. Linear shape functions are then used for the spatial finite element discretization.

4. Results and Discussion

4.1. Temporal discretization

Newmark and Hilber-Hughes-Taylor (HHT) schemes have been tested within the DSC framework. In figure 3 the trajectories on a transverse plane of a node placed at glottal exit, at $[0.0250, 0, -0.0369]$ at time $t = 0$, for different temporal discretization algorithms and time steps h. Discretizations at $h = 200$, 100 and $50\,\mu s$ are shown in blue, green and red lines, respectively. Solid lines correspond to a trapezoidal rule (TR), dot-dashed line to a modified average acceleration scheme (MAA) with $\gamma = 0.6$, dashed lines to a HHT method with $\alpha = -0.3$, and spaced-dashed line to a HHT method with $\alpha = -0.03$.

All schemes presented here are second-order accurate, except the MAA, which is first-order accurate. Even though the time steps are small, the effect of the discretization error is evident in figure 3 by the noticeable differences in amplitude. Assuming contact at the midsaggital plane, the error may lead to artificial collision. The error difference is minor between time steps $h = 100$ and $50\,\mu s$. It is worth noting that by reducing the time step by a factor of 0.5, the number of steps is double for each glottal cycle. As a consequence, the computational time is increased, which suggests that very small time steps are not desirable.

At $h = 200\,\mu s$ a first-order accurate MAA scheme presents an improved amplitude compared to a second-order TR scheme, since it approximates the amplitudes obtained at smaller time steps. This indicates that numerical dissipation of spurious high modal components is of importance. At the same time

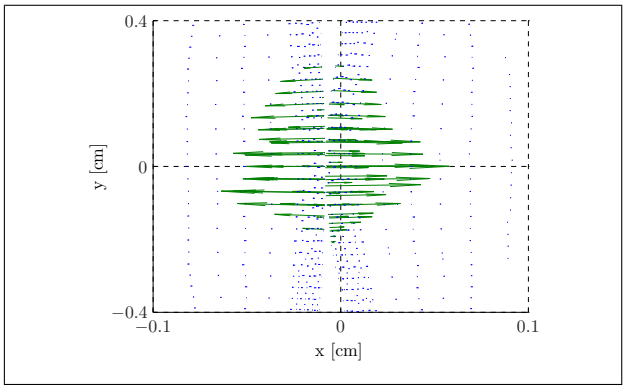

Figure 4. Transversal view of asymmetric vocal folds' collision. In blue, aerodynamic force; in green, contact forces with $k = 10^6$.

step, a better improvement is achieved by a HHT scheme with $\alpha = -0.3$, which makes evident the deficiency of a low-order accurate scheme. At $h = 100\,\mu s$, the amplitude difference between HHT schemes with $\alpha = -0.05$ and $\alpha = -0.3$, also than the similarities of the latter to the TR scheme at $h = 50\mu s$, confirm the need of introducing damping at high frequencies. Additionally, the fact that HHT method with $\alpha = -0.05$ and a dissipation-free TR method show more similarities than a HHT method with $\alpha = -0.05$, may indicate that slight damping of low modes is not of great relevance. Although results are improved at $h = 50\,\mu s$, it is worth noting that approximately the same amplitude is achieve by HHT scheme with $\alpha = -0.3$ at a larger step $h = 100\,\mu s$.

Accuracy of the algorithms may be also measured by the numerical dispersion introduced by the scheme. All methods presented here show an oscillation period of $204 - 206$ Hz, except at a time step $h = 200\,\mu s$ where the period is below 190 Hz. This may indicate that dissipation error is not relevant whenever other accuracy measures are favorable.

4.2. Contact Forces

All results presented in this and the following section use a HHT scheme for temporal discretization, with $\alpha = -0.3$ and $h = 100\,\mu s$.

Figure 4 shows the aerodynamic forces (in blue) and the contact forces (in green) at time $t = 23.3$ ms for an asymmetric vibration enforced by decreasing the left longitudinal Young's modulus of the body by 30%. Note the characteristic incomplete anterior and posterior glottal closure of vocal folds' dynamics, as reported in Ref. [26]. For the sake of simplicity, however, the flow is blocked when collision occurs close to the mid-coronal plane. Hence, the aerodynamic pressure is constant and equal to the subglottal pressure. The penetration between the two vocal folds is not visible, since the order of magnitude for the total interpenetration volume is less than -3. The collision detection mechanism for interface tracking described in

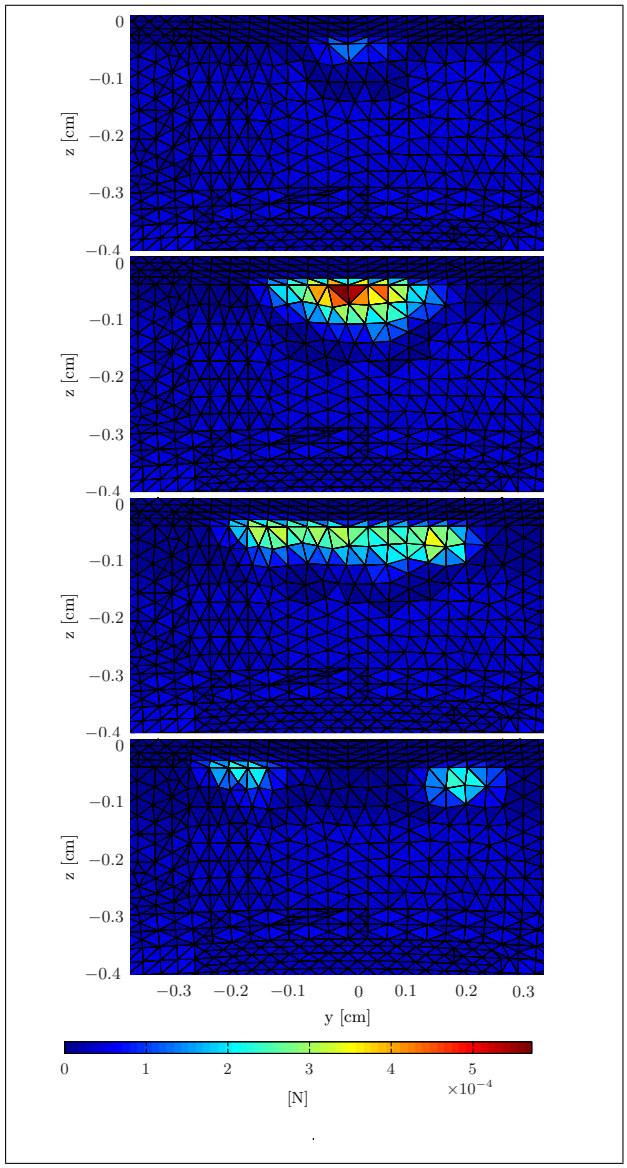

Figure 5. Saggital view of the colliding right vocal fold, for a symmetric parameter configuration, in increasing time step from top to bottom. In colors, the magnitude of the contact forces (x component) and aerodynamic forces acting on interface triangles.

section 2.3.1 appears to successfully detect midsaggital plane asymmetric impact.

Figure 5 shows the magnitude of the boundary forces acting on the colliding right vocal fold for a symmetric parameter configuration at times $t = 27.3$, 27.4, 27.5 and 27.6 ms from top to bottom, respectively. For each triangle, addition of the forces applied to the three nodal vertices has been used for the calculations. Note that above collision the force is zero, since no vocal tract coupling is introduced in this model. The wave-like behavior along the anteroposterior direction reported in the literature (see Ref. [8]) seems to agree with the displacement of the contact area as a function of time. Maximum contact force occurs at the mid-coronal plane, in agreement with the

studies presented in Ref. [23]. However, in this model the x component of the contact force acting on the entire contact area has a peak of 0.0311 N which exceed the value 0.01 N reported in Ref. [27]. This quantitative difference may be related to the model formulation, parameters or geometries; detailed investigations are needed in future studies.

4.3. Parameter study

It was mentioned earlier that asymmetric collision is relevant for clinical research. The functional imbalance between folds may be associated with either asymmetries in the initial boundary conditions conditions, or with asymmetries in the tissue parameters. The present model makes it possible to study asymmetric collision.

Figure 6 shows the normalized x-coordinate of the collision point of a node placed at $[0.0250, 0, -0.0369]$ at time $t = 0$, as a function of tension mismatch $100 \cdot (E_{right} - E_{left})/E_{right}$ between left and right longitudinal Young's modulus. The temporal mean over 8 steady cycles for the cover is shown in gray triangles, and the muscle in black circles, with the corresponding standard deviation as a vertical line. Note that a decrease on the left longitudinal Young's modulus (positive percentage of variation) leads to a shift of the collision point towards negative x-coordinates, suggesting that the amplitude of the left vocal fold is decreased. The mean in figure 6 shows that asymmetric collision is more sensitive to variations in the muscle, rather than in the cover. This may suggest that muscle tension imbalance is an unlikely cause of damage of functional voice disorders due to overuse of the voice, as endoscopy images are not clearly visually impaired [1]. Furthermore, the increasing standard deviation as a function of the percentage of left-right tension mismatch indicates that asymmetric collision introduces unsteadiness in vocal folds dynamics. Finally, note that for a symmetric parameter configuration, collision does not occur at the mid-coronal plane, suggesting that slight initial geometric asymmetries may be eventually involved in vibrational imbalance.

Figure 7 shows the magnitude of the maximum mediolateral compressive stress σ_{xx}, and the magnitude of the x component of the maximum contact force, as a function of tension mismatch between left and right longitudinal Young's modulus of the body. The stress tensor is calculated for each tetrahedral element, and it is constant due to the linear finite element discretization. The maximum is taken over one colliding cycle, within the left vocal fold. For a symmetric parameter configuration, the value of maximum compressive stress is within the range presented in Ref. [27]. The figure shows that asymmetries in the parameters affect the internal stress distribution. In agreement with figure 6, the maximum compressive stress on the left vocal fold decreases, since the collision point is shifted towards negative x components

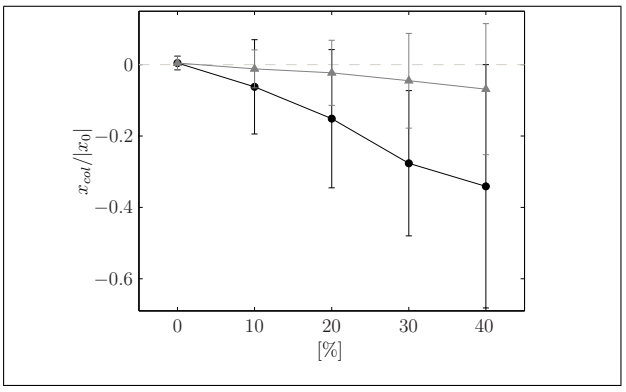

Figure 6. Collision point $x_{col}/|x_0|$ of a node placed at $[x_0, y_0, z_0] = [0.0250, 0, -0.0369]$ at time $t = 0$, as a function of the percentage of tension mismatch $100 \cdot (E_{right} - E_{left})/E_{right}$ between left and right longitudinal Young's modulus. In gray triangles, the cover; in black circles, the muscle. Marks indicate the temporal mean over 8 consecutive steady periods, and vertical lines the standard deviation.

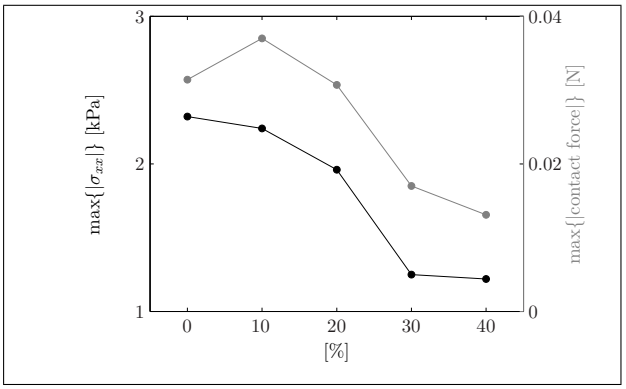

Figure 7. Magnitude of the maximum mediolateral compressive stress σ_{xx} in black, and contact force (x component) in gray over one colliding cycle, as a function of the percentage of tension mismatch between left and right longitudinal Young's modulus of the body. Results for the left vocal fold.

(left vocal fold position). The maximum magnitude of the contact force also decreases as a function of the percentage mismatch between parameters, except for a 10% mismatch, showing that vibrational imbalance has direct consequences on collision forces. This may suggest that damage between vocal folds with asymmetric tissue characteristics is not due to large impact forces.

5. Conclusions

In this paper a finite element model of the vocal folds with a fast fluid solver has been adapted to the Deformable Simplicial Complex mesh framework. A new approach for small deformations and frictionless contact of the vocal folds has been formulated and tested.

The importance of the accuracy of temporal integration schemes in vocal folds dynamics has been

shown. It can be concluded that high-frequency numerical dissipation appears to be of great importance, as well as the error introduced by the time step. The Hilber-Hughes-Taylor method with $\alpha = -0.3$ has been shown to be superior to Newmark schemes. Since a reduction of the calculation time is desired, an HHT method with $\alpha = -0.3$ at a time step of $h = 100\,\mu s$ seems to give accurate results. Additionally, numerical dispersion does not appear to play a role on accuracy measures.

The penalty approach combined with the novel deformable interface tracking used to enforce the kinematic collision constrains seems to successfully allow for asymmetric collision between vocal folds. Parameter studies indicate that marked asymmetric collision due tension imbalance is primarily related to impairments in the innermost layer. Mediolateral stress components as well as contact forces appear to be related to tension imbalance.

Acknowledgement

This research has been funded by the Swedish organization AFA Försäkring.

References

[1] V. L. Aahlander, R. Rydell, A. Löfqvist: Speaker's comfort in teaching environments: voice problems in Swedish teaching staff. Journal of Voice **25** (2011) 430–440.

[2] A. P. Pinheiro, D. E. Stewart, C. D. MacIel, J. C. Pereira, S. Oliveira: Analysis of nonlinear dynamics of vocal folds using high-speed video observation and biomechanical modeling. Digital Signal Processing: A Review Journal **22** (2012) 304–313.

[3] M. Spencer, T. Siegmund, L. Mongeau: Determination of superior surface strains and stresses, and vocal fold contact pressure in a synthetic larynx model using digital image correlation. The Journal of the Acoustical Society of America **123** (Feb. 2008) 1089–1103.

[4] R. Schwarz, U. Hoppe, M. Schuster, T. Wurzbacher, U. Eysholdt, J. Lohscheller: Classification of unilateral vocal fold paralysis by endoscopic digital high-speed recordings and inversion of a biomechanical model. IEEE Transactions on Biomedical Engineering **53** (2006) 1099–1108.

[5] J. Van Den Berg, J. T. Zantema, R. J. Doornenbal: On the Air Resistance and the Bernoulli Effect of the Human Larynx. Journal of the Acoustical Society of America **29** (1957) 626–631.

[6] J. Jansson: Adaptive stabilized finite element framework for simulation of vocal fold turbulent fluid-structure interaction and towards aeroacoustics. The Journal of the Acoustical Society of America **133** (2013).

[7] T. J. R. Hughes: The Finite Element Method: Linear Static and Dynamic Finite Element Analysis. Vol. 682. Dover Publications, 2000, (Dover Civil and Mechanical Engineering Series).

[8] F. Alipour, D. A. Berry, I. R. Titze: A finite-element model of vocal-fold vibration. Journal of the Acoustical Society of America **108** (2000) 3003–3012.

[9] M. D. O. Rosa, J. C. Pereira, M. Grellet, A. Alwan: A contribution to simulating a three-dimensional larynx model using the finite element method. Journal of the Acoustical Society of America **114** (2003) 2893–2905.

[10] M. K. Misztal, J. A. Baerentzen: Topology-adaptive interface tracking using the deformable simplicial complex. ACM Transactions on Graphics **31** (2012) 1–12.

[11] K. Ishizaka, K. Matsudaira: Fluid mechanical considerations of vocal cord vibration. Monogr. 8, Speech Commun. Res. Lab., Santa Barbara, CA., 1972.

[12] G. Z. Decker, S. L. Thomson: Computational simulations of vocal fold vibration: Bernoulli versus Navier-Stokes. Journal of Voice **21** (2007) 273–284.

[13] D. A. Berry, I. R. Titze: Normal modes in a continuum model of vocal fold tissues. Journal of the Acoustical Society of America **100** (1996) 3345–3354.

[14] P. Wriggers: Computational contact mechanics. John Wiley & Sons, 2002.

[15] O. Zienkiewicz: The finite element method. McGraw-Hill, 1977.

[16] N. J. Carpenter, R. L. Taylor, M. G. Katona: Lagrange constraints for transient finite element surface contact. International Journal for Numerical Methods in Engineering **32** (1991) 103–128.

[17] I. Steinecke, H. C. K. P. H. Herzel: Bifurcations in an asymmetric vocal-fold model. Journal of the Acoustical Society of America **97** (1995) 1874–84.

[18] B. Nouromid: A note on the optimum choice for penalty parameters. Communications in Applied Numerical Methods **3** (1987) 581 – 585.

[19] N. M. Newmark: A Method of Computation for Structural Dynamics. Journal of the Engineering Mechanics Division **85** (1959) 67–94.

[20] H. M. Hilber, T. J. R. Hughes, R. L. Taylor: Improved Numerical Dissipation for time Integration Algorithms in Structural Dynamics. Earthquake Engineering & Structural Dynamics **5** (1977) 283–292.

[21] M. K. Misztal, K. Erleben, A. Bargteil, J. Fursund, B. B. Christensen, J. Andreas Bærentzen, R. Bridson: Multiphase flow of immiscible fluids on unstructured moving meshes. IEEE transactions on visualization and computer graphics **20** (2014) 4–16.

[22] U. Bonde, V. Visseq, K. Erleben: Disjoint domains interactions framework for hyperelastic simulations. 11th World Congress on Computational Mechanics, 2014.

[23] C. Tao, J. J. Jiang, Y. Zhang: Simulation of vocal fold impact pressures with a self-oscillating finite-element model. Journal of the Acoustical Society of America **119** (2006) 3987–3994.

[24] X. Zheng, Q. Xue, R. Mittal, S. Beilamowicz: A coupled sharp-interface immersed boundary-finite-element method for flow-structure interaction with application to human phonation. Journal of Biomechanical Engineering **132** (2010) 111003.

[25] Q. Xue, R. Mittal, X. Zheng, S. Bielamowicz: A computational study of the effect of vocal-fold asymmetry on phonation. The Journal of the Acoustical Society of America **128** (2010) 818–827.

[26] Y. Pelorson, X. and Hirschberg, A. and van Hassel, R. R. and Wijnands, A. P. J. and Auregan: Theoretical and experimental study of quasisteady-flow separation within the glottis during phonation. Application

to a modified two-mass model. Journal of the Acoustical Society of America **96** (1994) 3416–3431.

[27] H. E. Gunter: A mechanical model of vocal-fold collision with high spatial and temporal resolution. Journal of the Acoustical Society of America **113** (2003) 994–1000.